Design of Artificial Hollow Moth-Eye Structures Using Anodic Nanocones for High-Performance Optics

Chia-Tien Wu,[†] Chun-Hung Lin,[‡] Chieh Cheng,[†] Chung-Shu Wu,[†] Huai-Chen Ting,[†] Feng-Chih Chang,[†] and Fu-Hsiang Ko*,[†]

[†]*Department of Materials Science and Engineering, National Chiao Tung University, Hsinchu 300, Taiwan, and* [‡]*Institute of Electro-Optical Science and Engineering, National Cheng Kung University, Tainan 701, Taiwan*

We demonstrated an innovative approach for the fabrication of self-organized, hollow-to-solid nanocone arrays, using a decoupling two-step anodization of an Al/Ta interlayer on a substrate. The porosity of the hollow nanostructures was tunable by the deposited thickness of Ta film. We also employed subwavelength nanocone arrays as Moth-eye structures for high-performance antireflection coatings. These oxide nanostructures greatly suppressed reflectance over a large range of wavelengths and angles of incidence and displayed a good mechanical stability. When a corresponding porosity was designed, these nanostructures could be applied to various substrates for an effective antireflection coating. In addition, we were able to customize antireflection coatings for various types of substrates or materials of interest based on the suitable coating of initial Ta thickness.

Antireflection (AR) coating is one of the most important optical designs, and it makes up more than 50% of the total optical thin-film market.[1] It is used to suppress surface reflection and to increase transmission of light for optical applications, such as flat panel displays, lasers, photovoltaic devices, and all kinds of lenses. Rayleigh first observed a thin film whose refractive index (n) is the geometric mean of the air, and then, substrate's indices reduced the reflection on the surface of the substrate optimally. In the early 19th century, interference AR coating was discovered using one-quarter of the light's wavelength in thickness. Thus, a single layer structure was applied in general AR coatings by following the aforementioned two conditions, but it only works at a specific wavelength and a normally incident light source. Over the past few decades, the AR coatings primarily consisted of multilayer coatings comprising layers of high- and low-n. Through the algorithm design, multilayer coatings were applied to achieve a wider broadband AR across a visible region for incident angles ranging from 0° to 50°.[2] However, complicated stacks and unsatisfied angle-independence ability on multilayer AR coatings forced scientists to develop next-generation AR structures for future optical devices.

According to optical theory, the refractive index of the AR layer should gradually decrease from air to the substrate.[3] Apparently, the refractive index of any dense material is not small enough, but nature provides a solution for such antireflective structures (ARS). The moth eye consists of quasi-close-packed nipples having heights and spacings typically of less than 300 nm, which reduces reflection from it's compound eyes.[4] The ARS on the corneas of these insects gradually match the optical impedance of one medium with its neighbor across the interface.[5] This concept has been applied to realize a variety of photonic systems, particularly semiconductor photovoltaic devices. Many techniques based on top-down etching like lithography,[6] self-organized templates,[7−9] and mask-less etching[10,11] have been used to fabricate tiplike nanostructure for ARS surfaces. Other ARS surfaces based on bottom-up growth like conical nanorods fabricated by the vapor−liquid−solid (VLS) method[12,13] and oblique-angle deposition[14,15] also succeed in enhancing light

---

*To whom correspondence should be addressed. E-mail: fhko@ mail.nctu.edu.tw.

(1) Liou, Y. Y.; Wei, Z. W.; Wang, L. R.; Liu, C. C.; Kuo, C. C.; Jaing, C. C.; Lee, C. C. *Opt. Rev.* **2009,** *16,* 176–179.
(2) Hannon, J. P.; Hung, N. V.; Trammell, G. T.; Gerdau, E.; Mueller, M.; Ruffer, R.; Winkler, H. *Phys. Rev. B* **1985,** *32,* 5068–5080.
(3) Kikuta, H.; Toyota, H.; Yu, W. J. *Opt. Rev.* **2003,** *10,* 63–73.
(4) Kunze, P.; Hausen, K. *Nature* **1971,** *231,* 392–393.
(5) Wilson, S. J.; Hutley, M. C. *Opt. Acta* **1982,** *29,* 993–1009.
(6) Boden, S. A.; Bagnall, D. M. *Appl. Phys. Lett.* **2008,** *93,* 133108.
(7) Zhu, J.; Yu, Z.; Burkhard, G.; Hsu, C. M.; Connor, S. T.; Xu, Y.; Wang, Q.; McGehee, M.; Fan, S.; Cui, Y. *Nano Lett.* **2009,** *9,* 279–282.
(8) Chuang, S. Y.; Chen, H. L.; Shieh, J.; Lin, C. H.; Cheng, C. C.; Liu, H. W.; Yu, C. C. *Nanoscale* **2010,** *2,* 799–805.
(9) Hao, J. Y.; Lu, N.; Xu, H. B.; Wang, W. T.; Gao, L. G.; Chi, L. F. *Chem. Mater.* **2009,** *21,* 1802–1805.
(10) Huang, Y. F.; Chattopadhyay, S.; Jen, Y. J.; Peng, C. Y.; Liu, T. A.; Hsu, Y. K.; Pan, C. L.; Lo, H. C.; Hsu, C. H.; Chang, Y. H.; Lee, C. S.; Chen, K. H.; Chen, L. C. *Nat. Nanotechnol.* **2007,** *2,* 770–774.
(11) Shieh, J.; Lin, C. H.; Yang, M. C. *J. Phys. D: Appl. Phys.* **2007,** *40,* 2242–2246.
(12) Yu, P. C.; Chang, C. H.; Chiu, C. H.; Yang, C. S.; Yu, J. C.; Kuo, H. C.; Hsu, S. H.; Chang, Y. C. *Adv. Mater.* **2009,** *21,* 1618–1621.
(13) Chueh, Y. L.; Fan, Z. Y.; Takei, K.; Ko, H.; Kapadia, R.; Rathore, A. A.; Miller, N.; Yu, K.; Wu, M.; Haller, E. E.; Javey, A. *Nano Lett.* **2010,** *10,* 520–523.
(14) Chhajed, S.; Schubert, M. F.; Kim, J. K.; Schubert, E. F. *Appl. Phys. Lett.* **2008,** *93,* 251108.
(15) Xi, J. Q.; Schubert, M. F.; Kim, J. K.; Schubert, E. F.; Chen, M.; Lin, S. Y.; Liu, W.; Smart, J. A. *Nat. Photonics* **2007,** *1,* 176–179.

---

coupling in solar cells or more efficient light extraction from LEDs.

For optical transparencies with low-n (e.g., glass or quartz), it remains a challenge to improve the transmission over a broad wavelength and incidence using ARS. Unlike Si and other semiconductor materials, these transparent substrates are arduous to etch anisotropically and selectively. Few ARS surfaces on fused silica or glass have been reported recently.[16,17] For the low-cost and large-scale fabrication, hence, porous polymer films have been developed to achieve ideal AR efficiency. Walheim et al. and Ibn-Elhaj et al. pioneered in nanocorrugated surfaces by removing one component of phase-separated polymer films and showed improved transmittance as high as 99%.[18,19] A further nanoporous multilayer film with a gradual porosity ratio for each layer demonstrated an advantage in omnidirectional reflection of incident light.[20,21] Other hybrid porous films composed of nanoparticles and polymer matrix were assembled by a layer-by-layer (LBL) technique and also resulted in an increase of light transmission.[22,23] Nevertheless, polymer-based ARSs continue to exhibit several fundamental problems, such as layer ablation and surface abrasion. In addition, polymer-based materials suffer from thermal decomposition at a high temperature and/or radiation damage when subjected to ultraviolet light.

Porous anodic alumina (PAA), formed from films on substrates directly, is an extremely versatile template for the growth of many nanostructures. If a metal whose oxide form has a higher ionic conductivity than alumina was used as an underlayer preceding an Al anodization process, the underlying metal would be also oxidized and thereby form metal−oxide nanostructures with a similar pattern as the upper PAA.[24−28] The oxides of Ti, Ta, Nb, and W are known to penetrate the barrier layer of PAA and grow into nanodot or nanorod arrays. In this study, we investigated a new approach to manipulate the above oxide nanostructures into periodic arrays of hollow-to-solid nanocones and serve as artificial moth-eye structures for high-performance ARS. An increase in porosity of the nanostructure, which corresponds to a decrease in effective-n, could lead to a broadening of antireflective ability for a universal substrate. The nanocone array (NCA) structure dramatically reduced the surface reflection over broadband wavelengths even at large angles on glass, which resulted from a gradient in the refractive index between air and the substrate. Also, NCA coatings exhibited a good mechanical stability and an effective AR ability on sapphire and AlN substrates.

Materials and Methods

Chemicals and Materials. Phosphoric acid (H_3PO_4, 86%), anhydrous ethanol (99.5%), and dihydrate oxalic acid ($C_2H_2O_4 \cdot 2H_2O$, 99.8%) were purchased from J. T. Baker (Phillipsburg, NJ, USA). Chromium trioxide (CrO_3, 99%) and perchloric acid ($HClO_4$, 70%) were purchased from Showa (Tokyo, Japan). Aluminum nitride substrate (AlN, 99.95%) and Pyrex 7740 glass were purchased from Corning (Corning, NY, USA). Tantalum target (99.995%) and aluminum slugs (99.995%) were purchased form Praxair (Danbury, CN, USA). Ultrapure water used in all experiments was purified with a Milli-Q apparatus (Millipore, Billerica, MA, USA) to a resistivity of 18.2 MΩ cm. All chemicals were used without further purification.

Al/Ta Bilayers Preparation. The tantalum film was deposited onto cleaned borosilicate glass (Pyrex 7740) and AlN and sapphire substrates by an ultrahigh vacuum DC sputtering system (ULVAC, SBH-3308). Before film deposition, the base pressure of the sputtering chamber was adjusted to approximately 5×10^{-7} Torr. Subsequently, the sample was followed by deposition of an aluminum film (5 μm) using thermal evaporation (ULVAC EBX-6D) in a high vacuum chamber (2×10^{-6} Torr). The Al/Ta sample then was electrochemically polished in a vigorously stirred 1:4 mixture solution of $HClO_4$ and ethanol (1 °C) at fixed 20 V in order to reduce the surface roughness during high-field anodization.

Anodization. Anodization was performed in a glass beaker cooled by a powerful cooling system with vigorous magnetic stirring and maintained at the temperature of 1 °C. A DC power supply connected to a computer system was used to control the variations of potential and current during anodization. A Cu foil was used as the support for the working electrode. The substrate was positioned on top of the support while Cu tapes were used to connect the Cu support to the Al film upon the sample. Two acrylic caps were used to fasten the sample and the Cu support inside within the O-ring. A graphite flake was used as the counter electrode.

A process called decoupling two-step anodization[29] was used to obtain an ordered array and a period of 200 nm. This approach was based on changing the electrolyte in the second step, while applying the same voltage as the first step. The preanodization step at a constant voltage of 40 V in 0.3 M oxalic acid for 3 min produced a thin porous oxide layer (about 200 nm) on the surface.[30] Then, the anodization voltage was gradually increased to a target formation voltage (110 V) at the rate of 1 V s^{-1}. At the first step of hard anodization for 5 min, a 4 μm-thick aluminum was converted into porous alumina. Then, the alumina film was removed using a solution of 5 wt % H_3PO_4 and 45 g L^{-1} chromic acid at 50 °C for 15 min. At the second step, mild anodization was anodized at same voltage of 110 V in 1.0 M phosphoric acid solution. After the current decreased into a background level

(16) Lohmuller, T.; Helgert, M.; Sundermann, M.; Brunner, R.; Spatz, J. P. *Nano Lett.* **2008**, *8*, 1429–1433.
(17) Li, Y. F.; Zhang, J. H.; Zhu, S. J.; Dong, H. P.; Jia, F.; Wang, Z. H.; Sun, Z. Q.; Zhang, L.; Li, Y.; Li, H. B.; Xu, W. Q.; Yang, B. *Adv. Mater.* **2009**, *21*, 4731–4734.
(18) Walheim, S.; Schaffer, E.; Mlynek, J.; Steiner, U. *Science* **1999**, *283*, 520–522.
(19) Ibn-Elhaj, M.; Schadt, M. *Nature* **2001**, *410*, 796–799.
(20) Li, X.; Gao, J. P.; Xue, L. J.; Han, Y. C. *Adv. Funct. Mater.* **2010**, *20*, 259–265.
(21) Park, M. S.; Kim, J. K. *Langmuir* **2005**, *21*, 11404–11408.
(22) Wu, Z.; Walish, J.; Nolte, A.; Zhai, L.; Cohen, R. E.; Rubner, M. F. *Adv. Mater.* **2006**, *18*, 2699–2702.
(23) Faustini, M.; Nicole, L.; Boissiere, C.; Innocenzi, P.; Sanchez, C.; Grosso, D. *Chem. Mater.* **2010**, *22*, 4406–4413.
(24) Mozalev, A.; Sakairi, M.; Saeki, I.; Takahashi, H. *Electrochim. Acta* **2003**, *48*, 3155–3170.
(25) Chu, S. Z.; Inoue, S.; Wada, K.; Hishita, S.; Kurashima, K. *Adv. Funct. Mater.* **2005**, *15*, 1343–1349.
(26) Wu, C. T.; Ko, F. H.; Hwang, H. Y. *Microelectron. Eng.* **2006**, *83*, 1567–1570.
(27) Devan, R. S.; Ho, W. D.; Lin, J. H.; Wu, S. Y.; Ma, Y. R.; Lee, P. C.; Liou, Y. S. *Cryst. Growth Des.* **2008**, *8*, 4465–4468.
(28) Oh, J.; Thompson, C. V. *Adv. Mater.* **2008**, *20*, 1368–1372.

(29) Lee, K. H.; Wong, C. C. *J. Appl. Phys.* **2009**, *106*, 104305.
(30) Lee, W.; Ji, R.; Gosele, U.; Nielsch, K. *Nat. Mater.* **2006**, *5*, 741–747.

and remained past 1 min, the nanostructure by the anodization method was obtained.

Characterization. The morphology was observed by field-emission scanning electron microscopy (JEOL, JSE-6700F) and field-emission transmission electron microscopy (JEOL, JEM-2100F). The XPS employed to analyze the chemical composition in depth profiles was performed on a Physical Electronics ESCA PHI1600 system with Al Kα excitation. The reflectance and transmittance were measured by a variable-angle optical spectrometer (Hitachi, U-4100) with an integrating sphere. The refractive index was confirmed by a variable-angle spectroscopic ellipsometer. RCWA (rigorous coupled-wave analysis)[11] was used to simulate the optical properties of these three-dimensional nanostructures (for details, see Supporting Information, Figure S1).

Mechanical Test. After NCAs were fabricated on AlN and sapphire substrates, a serial test including abrasion, corrosion, and temperature resistance was acquired. In the beginning, abrasion resistance was performed on a Taber 5750 abraser according to the ASTM standard. The test involved 100 cycles of abrasion using a CS10-F resilient wheel with a 350 g load. Next, corrosion resistance was performed in a 2 M H_2SO_4 solution at a temperature of 60 °C for 2 h. Finally, a high temperature test was conducted in a furnace with a heating rate of 5 °C/min, and the temperature was kept at 800 °C for 2 h.

Results and Discussion

Synthesis, Characterization, and Formation Mechanism of NCAs. In contrast to conventional PAA processes, a decoupling two-step anodization including the hard anodization (HA) and the mild anodization (MA) was used to achieve an ordered array and an ideal period in this study. The HA in the first step established a fast and well-ordering regime with interpore distances of 200 nm, which could not be obtained through mild anodization processes. A 200 nm period satisfied the zero-order condition in glasses considering internal reflections,[31] and the simulated NCA with a period of 200 nm and a height of 200 nm were optimized to the ideal transmittance from RCWA simulation (see Supporting Information, Figure S2). According to the prior report,[30] the current density is inversely proportional to the exponent of barrier thickness for a given anodization voltage. The great current density in the HA resulted in a thick barrier that makes it difficult for the nanostructure to penetrate the alumina barrier and grow into the alumina pores. To solve this key problem, the MA process in the second step was used to provide a thin barrier for NCA structure growth and preserve the ordering and pore distance inherited from the first HA step.

Figure 1 recorded chronoamperical curves during the second mild anodization of Al on glass substrates within t_{Ta} (the deposited thickness of Ta film) = 0, 10, and 30 nm which represented the growth of general PAA, hollow NCA, and solid NCA structures, respectively. At the first stage, the current drops were initially due to barrier layer formation, followed by an escalation in current. During anodization of the Al/glass sample, it was found that the current saturated after the alumina barrier had reached
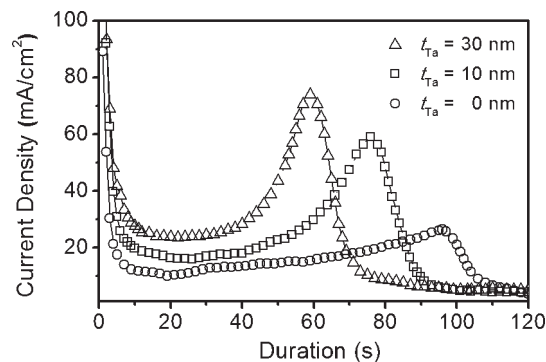
(31) Song, Y. M.; Choi, H. J.; Yu, J. S.; Lee, Y. T. *Opt. Express* **2010**, *18*, 13063–13071.

Figure 1. Typical chronoamperical curve, recorded during the anodization of Al on glass substrates where t_{Ta} = 0 nm (general PAA), 10 nm (hollow NCA structure), and 30 nm (solid NCA structure).

the interface, and an inverted U-shape was formed.[32] For Ta interlaid samples, when the oxide barrier layer at the bottom of the pore approached the Ta−Al interface, anodization of the underlying Ta started. Since Ta had higher ionic conductivity than Al (comparing 1.8 with 1.0 nm V^{-1} for Ta_2O_5 and barrier layer of Al_2O_3 under similar anodization),[33] anodic tantalum oxide formed preferentially and responded by an increasing surge of current density. The increase in t_{Ta} brought about the larger current density due to better conductivity and in turn shortened the anodization time. Successively, the currents would decrease gradually and a visible change in color of the sample from opaque to transparency could be observed. Once anodization was completed, the values for current density dropped considerably and remained at a background level. It should be noted that with chronoamperical curves of the anodization in corresponding t_{Ta} on insulating glass, AlN and sapphire substrates revealed an identical feature and magnitude, depending on the electric conductivity of substrates.[34]

As shown in Figure 2, the average geometric features of our tantala NCAs were a period of 200 nm, a base diameter of 200 nm, a height of 200 nm, and a density of 2×10^9 cm^{-2}. These quasi-closely packed taper nanostructures, featuring a surface-relief grating and a period smaller than any of the wavelengths of visible light, served as Moth-eye structures. Cross-sectional TEM images reveal that clearly recognizable hollow-to-solid nanocones formed from Ta films that had initial thicknesses of 10 nm (Figure 2c), 20 nm (Figure 2d), and 30 nm (Figure 2e), respectively. An isolated nanostructure was embedded at the bottom of each alumina pore, i.e., at the interface between the porous alumina and the substrate. The tilt and cross-sectional images of NCAs display the tapered profile which benefits the corresponding gradient change in the refractive index. An interesting decline in porosity with increasing thickness of initial Ta was found, which corresponded to an increase in the solid part of tantalum oxide. The

(32) Li, F. Y.; Zhang, L.; Metzger, R. M. *Chem. Mater.* **1998**, *10*, 2470–2480.
(33) Sloppy, J. D.; Macdonald, D. D.; Dickey, E. C. *J. Electrochem. Soc.* **2010**, *157*, C157–C165.
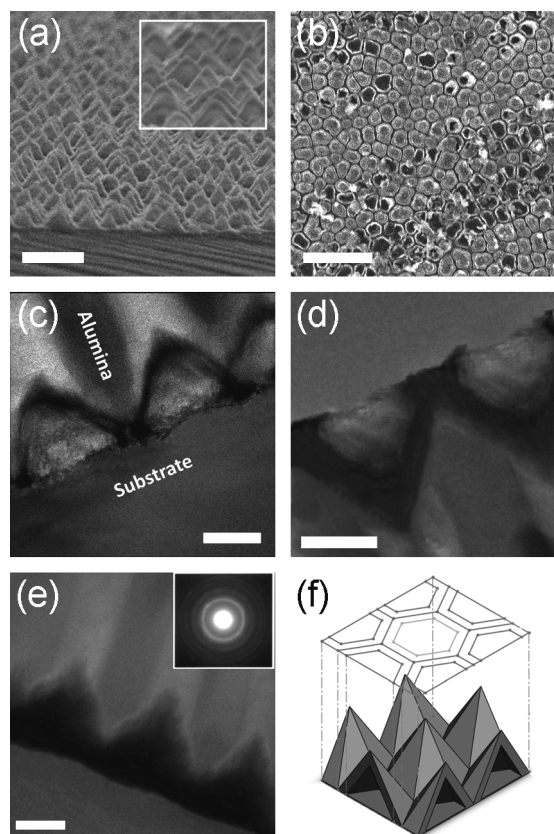(34) Foong, T. R. B.; Sellinger, A.; Hu, X. *ACS Nano* **2008**, *2*, 2250–2256.

Figure 2. SEM and TEM images of conelike nanostructure arrays. (a) Side view SEM image (scale bar: 500 nm) of hollow NCA after alumina had been removed selectively. Inset: Magnified image. (b) Top-view SEM image (scale bar: 1 μm) of hollow NCA that had been ground using a diamond emery paper. TEM images of hollow (c), (d) and solid (e) nanostructures under porous alumina (scale bar: 100 nm). Inset (e): SAED pattern revealing the amorphous composition. (f) Schematic representation of a close-packed hexagonal NCA for theoretical calculation: period, 200 nm; base diameter, 200 nm; height, 200 nm.

outer morphology of nanocones was almost the same from electron microscopy observation.

Currently, the mechanism of metal-oxide nanostructures formed between the pores of PPA, and the substrate was referred to the oxidation of metal layer.[26,28,35] The O^{2-} ions migrating inward through the alumina barrier layer were injected into the metal layer, and the metal-oxide nucleus was formed, as shown in Figure 3a. The growth (volume expansion) of the metal-oxide nanostructure resulted from the continuous combination of O^{2-} and metal ions. However, unlike those cases of solid nanostructure, our thin metal film of $t_{Ta} = 10$ nm was insufficient for oxidation. The excessive O^{2-} ions, relative to the limited Ta^{5+} ions, combined themselves to release oxygen gas at the anode. The gaseous oxygen, acting as a porogen, exerted great pressure to expand the tantalum oxide hillocks and left a void between them and the underlying substrate (Figure 3b). The stress produced by the oxygen was observed in the formation of the void under the pore of anodic PPA.[36] As the voids expanded as a result of the effects of gaseous oxygen, the barrier layers eventually
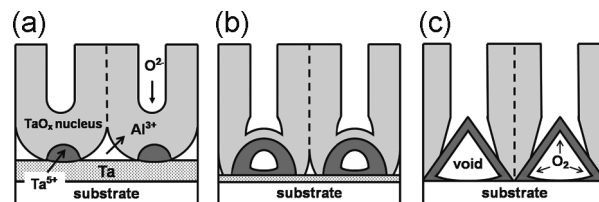

Figure 3. Schematic representation of the mechanism of the formation of the hollow nanocones. (a) Tantalum oxide nucleus formed as the anodization approached the Ta−Al interface. (b) Tantalum oxide hillocks grew, leaving voids caused by oxygen pressure. (c) Conelike hollow nanostructures formed with pore wall obstruction.

dissolved entirely and the hollow hillocks grew upward. With pore-wall obstruction, the conelike hollow nanostructures were ultimately obtained (Figure 3c). Like our previous report of solid NCA,[35] the outer shape of nanocones was not affected by t_{Ta} because it was restricted by the alumina pore wall. It was, however, strongly dependent on the anodizing parameters. We also noted that the distance between nanocone bases was approximately 0 nm, which is much smaller than other similar tantala nanostructures fabricated by anodizaion of Al/Ta bilayer.[24,26,27] We supposed that the key was the deposited thickness of metal film. The thick metal films (> 100 nm) in previous work[37] led to the incomplete oxidation of underlying metal, which suppressed the transverse expansion of nanostructures.

The porosity of the hollow nanostructures was tuned by varying the deposited thickness of Ta film. Increasing t_{Ta} from 10 to 30 nm led to a significant decrease in the porosity of nanocones, which turned into a solid structure from a hollow one, as seen in Figure 2c−e. The porosities of hollow nanostructures for the samples of $t_{Ta} = 10$ and 20 nm were estimated to be 69.8% and 35.5% upon TEM images while a solid nanostructure was presented for the sample of $t_{Ta} = 30$. More accurate methods for calculating porosity could be implemented by the Pilling-Bedworth (PB) ratio defined as the ratio of the volume of the metal oxide produced by the reaction of metal and oxygen to the consumed metal volume. Assuming all metal Ta was transformed into tantalum oxide, a hexagonal close-packed array as shown in Figure 2f, the value of R_{PB} is expressed theoretically by the following equation:

$$R_{PB} = \frac{V_{metal\_oxide\_produced}}{V_{metal\_consumed}} = \frac{V_{solid\_pyramids}}{V_{Ta\_film}}$$

$$= \frac{Ah(1-P)/3}{At_{Ta}}$$

where A, h, and P are the based area, the height, and the porosity of nanocones, respectively. R_{PB} of Ta anodization has been reported as 2.3;[38] then, the relationship between t_{Ta} and porosity is given by $1 - 0.0345\ t_{Ta} = P$. Hence, the calculated porosities of $t_{Ta} = 10$ and 20 nm were 65.5% and 31.0%, which are in agreement with the values of TEM observations. Knowledge of t_{Ta} and

(35) Wu, C. T.; Ko, F. H.; Lin, C. H. *Appl. Phys. Lett.* **2007**, *90*, 171911.
(36) Chu, S. Z.; Wada, K.; Inoue, S.; Todoroki, S. *J. Electrochem. Soc.* **2002**, *149*, B321–B327.
(37) Gong, J.; Butler, W. H.; Zangari, G. *J. Mater. Chem.* **2008**, *18*, 1741–1746.
(38) Mardilovich, P.; Kornilovitch, P. *Nano Lett.* **2005**, *5*, 1899–1904.

Article

Chem. Mater., Vol. 22, No. 24, 2010 6587

corresponding porosity is needed to determine how much Ta should be deposited initially to obtain a desired porosity that will alter the photonic properties of NCAs.

In order to obtain the insight into the chemical composition of NCAs, XPS depth profiling analysis was performed for the anodized samples after selectively removing the exposed PAA by mixed chromic and phosphoric acid for 10 min. Ar^+ sputtering of 60 and 6 min was used to examine the inner composition of respective solid and hollow NCAs. Each sputter cycle lasted 1 min, which was estimated to remove a 2 nm film of dense anodic tantalum oxide. The measured spectra were calibrated using a Shirley background subtraction. Binding energies were referenced to the carbon−hydrogen peak at 285.0 eV. The Ta^{5+} 4f spectrum consisted of two doublet peaks ($4f^{7/2}$ and $4f^{5/2}$) with binding energies at 26.5 and 28.4 eV, respectively. The analysis in Figure 4 revealed that the Ta 4f lines were almost composed of Ta^{5+} 4f peaks, which indicates the formation of tantalum oxide referred to as stoichiometric Ta_2O_5. The suitable control of thickness (t_{Ta}) avoided the formation of unoxidized tantalum and suboxides (TaO or TaO_2)[27] which are commonly manifested in anodic nanostructures from thick metal films. The measured results confirmed mostly the stoichiometric Ta_2O_5 in the depth of hollow and solid NCAs. Our approach is very efficient to avoid the problem of formation metal-Ta residual that could cause the reduction of antireflective ability.

Antireflection Properties of NCAs. We employed our developed subwavelength NCAs as antireflection coatings on Pyrex glass substrates. The optical performance of the antireflection surfaces exhibited here was evaluated by transmission, wavelength, and variable-angle reflection measurements, respectively. An integrating sphere was used in the measurement to collect the diffuse and specular reflectance from all directions. We used $t_{Ta} = 10$ nm on one side of the substrates to fabricate hollow NCA plus $t_{Ta} = 20$ and 30 nm for comparison. Figure 5a provides their measurements with that of bare glass. It is found that not all spectra resulted in positive antireflection properties in the total transmission across the spectral range from 300 to 900 nm. In the case of 10 nm initial Ta, the transmissions of the glass substrates coated with hollow NCA increased across the whole visible range homogeneously. On account of the reflection of the back side, a double-sided coating of $t_{Ta} = 10$ nm was applied to ideal antireflective properties; it provided an average transmittance of 97.8% and a maximum transmittance of 98.2% at 480 nm while the transmission of a blank substrate was < 92.5%.

One advantage of having a smooth and continuous gradient in *n*-profile is that it results in the reflection of incident light over wide angles.[3] To verify the omnidirectional characteristics, we performed comparisons of specular reflectance as a function of wavelength in the visible range from 400 to 800 nm and angles of incidence from 30° to 70° (Figure 5b). Generally, the reflectance for coated or uncoated samples is insensitive to the incidence angle from 0° to 30°. For the incidence angle up to 45°, the
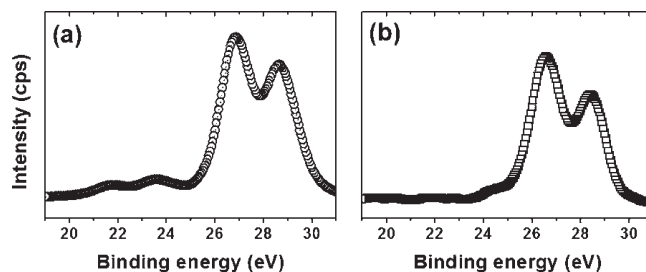

Figure 4. XPS depth-profile analysis of tantalum oxide NCAs on glass substrates at normal incidence. (a) Ta 4f spectrum of solid NCA ($t_{Ta} = 30$ nm); (b) Ta 4f spectrum of hollow NCA ($t_{Ta} = 10$ nm).
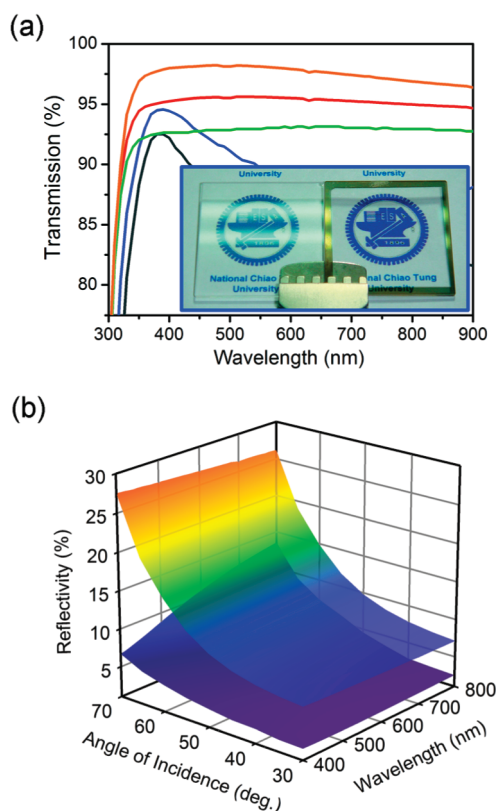

Figure 5. Optical performance of antireflective properties for NCA-coating glasses. (a) Measured transmissions of bare glass (green line) and NCA-coated (single side) glass substrates of initial Ta thicknesses of 10 nm (red line), 20 nm (blue line), 30 nm (black line), and 10 nm for double sides (orange line). Inset: Photographs of the structured (right) and unstructured (left) glass samples (30 mm × 30 mm) demonstrate the antireflective effect at a large tilted angle. (b) Measured wavelength and angle resolved absolute reflectance. The glass substrates were coated without (upper curve) and with double-sided NCA coating (lower curve).

specular reflectance of double-sided NCA coatings exhibits a result below 3% over a spectral range from 400 to 800 nm, while it is above 7.5% for a planar glass substrate. Unlike the quasi-thin-film coatings prepared from porous materials or particles, our conelike nanostructures provide broadband antireflective ability over large incident angles. The average reflectivities of coated and uncoated glasses for an incident angle of 70° are 10.3% and 26.4%, which improved over the whole visible spectrum with an average factor of 16%. The inserted photography of our University's Logo in Figure 5a supports the result of antireflection properties with a large tilted angle. Two glass substrates with and without NCA coating were
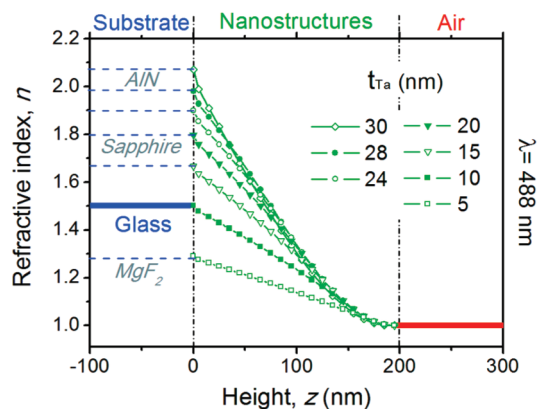
Figure 6. Refractive index profiles (for samples of various t_{Ta}) through air, the nanostructure, and the substrate (wavelength: 488 nm). The horizontal axis represents the distance from the interface of the nanostructure and the substrate.

exposed to daylight lamps. The glass substrate on the left (without coating nanostructure) revealed the problem of ghost images from the light for oblique incident angles. On the contrary, the glass at the right side with coating our developed nanostructure demonstrated fine suppression of the light reflection. Also, the improvement of transmission was identical to a virtual elimination of reflectance over the visible spectrum, which means no scattering and absorption impairment was caused by the hollow nanostructures.

To understand why the hollow interiors of the NCAs improved the transmission, the refractive index profile via different t_{Ta} has to be established (Figure 6) by effective medium approximations[3] (see Supporting Information, Figure S3). The obtained taper structure was assumed to be a hexagonal close-packed period of 200 nm and a height of 200 nm (like in Figure 2f), which was divided vertically in terms of gradient size. For uncoated glass substrate (t_{Ta} = 0 nm), the n leaps abruptly from 1.0 to 1.502 (at 488 nm) across the air/glass interface, causing unnecessary reflection. The gradual change of n from air to substrate is crucial for ideal antireflection properties. The coated sample with t_{Ta} = 10 nm (P = 65.6%) in Figure 6 exhibits the smoothest n change from the air to the substrate, thereby showing the maximum transmission. In other cases of t_{Ta}, in fact, NCA coatings also provide the graded-n-profile for specific substrates due to the different porosity. For example, a value of t_{Ta} of 5 nm (P = 82.8%) in Figure 6, when its effective-n changes continuously from 1.0 to 1.32, is suitable for an MgF_2 substrate. Obviously, we can customize antireflection coatings for various types of substrates or materials of interest based on the corresponding value of initial Ta thickness.

We also employed NCAs from t_{Ta} = 20 and 30 nm on sapphire and AlN substrates because they seemed to be the satisfactory AR coatings according to the n-profile in Figure 6. Additionally, to evaluate the mechanical stability and possible passivation behavior of the NCA coating, a serial test including abrasion, corrosion, and temperature resistance was acquired. The specular reflection
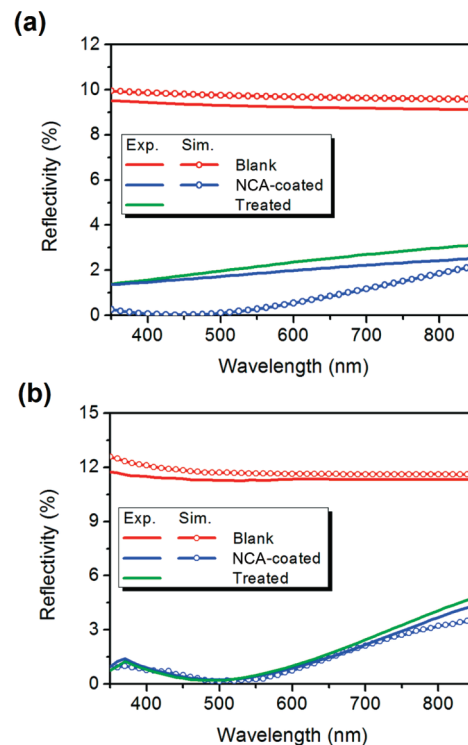

Figure 7. Improvement of reflectivity before and after the treatment for NCA coated on (a) sapphire and (b) AlN substrates. Experimental (solid) and RCWA-simulated (dotted) specular reflectivities at normal incidence were compared for a blank substrate (red lines), NCA coating (blue line), and NCA coating with treatment (green line).

was measured at an incidence angle of 5°. The resultant reflectance (Figure 7), which revealed a very close value before the treatment, also improved the reflectivity significantly. These findings render strong evidence for advantages in mechanical properties compared to other ARS coatings based on nanoparticle or polymer corrugation on transparent substrates. We supposed that it is very likely for NCA coatings to be used as general protective coatings for optical transparency. The experimental reflectance was further complemented by theoretical calculation using a 3-D rigorous coupled wave analysis (RCWA) model, and it agreed reasonably well with the simulated reflectivity on both samples.

Conclusions

In summary, artificial Moth-eye structures using hollow-to-solid nanocones were successfully fabricated for high-performance AR coatings. Quasi-closely packed arrays of conelike nanostructures were fabricated by decoupling two-step anodization of Al/Ta bilayers coated on substrates. We proposed the mechanism of formation of the hollow NCA due to the stress of gaseous oxygen. The tunable porosity of the hollow nanostructures was controlled by varying the deposited thickness of Ta film. The transmissions of the glass substrates coated with hollow NCA of 65.5% porosity reached greater than 97.8% over the whole visible range. Besides, the reflectivity was suppressed greatly in a broadband omnidirection and reached as low as 10% at an incident angle of 70°. In other cases of porosity,

Article

Chem. Mater., Vol. 22, No. 24, 2010 6589

NCA coatings were also found to be an efficient ARS on sapphire and AlN substrates. Good mechanical stability makes NCA suitable for protective coatings for optical transparency. The tunable availability of the hollow nano-structures has allowed for the design of artificial optical properties as new building blocks (e.g., diffractive layer, diffusers, or reflectors) in future photonic devices.

Supporting Information Available: Details of effective medium approximations and rigorous coupled wave analysis (PDF). This material is available free of charge via the Internet at http://pubs.acs.org.